

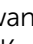






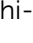






Cite this: DOI: 10.1039/d5el00031a

# Interface engineering of co-evaporated Sb<sub>2</sub>Se<sub>3</sub> solar cells using an ALD SnO<sub>x</sub> interlayer

Van-Quy Hoang,  <sup>†ab</sup> Jaebaek Lee, <sup>†a</sup> Geumha Lim, <sup>c</sup> Amanat Ali,  <sup>d</sup> Bashiru Kadiri-English,  <sup>d</sup> Dong-Hwan Jeon,  <sup>a</sup> Dae-Ho Son,  <sup>a</sup> Hyo Jeong Jo, <sup>a</sup> Dae-Kue Hwang,  <sup>a</sup> Kee-Jeong Yang,  <sup>a</sup> Eunkyung Cho,  <sup>a</sup> Jin-Kyu Kang,  <sup>a</sup> William Jo,  <sup>\*c</sup> Shi-Joon Sung  <sup>\*ad</sup> and Dae-Hwan Kim  <sup>\*ad</sup>

To compensate for the limited efficiency of co-evaporated Sb<sub>2</sub>Se<sub>3</sub> solar cells, effective physical and chemical passivation of the interface between the Sb<sub>2</sub>Se<sub>3</sub> absorber and the CdS buffer layer was achieved through the deposition of an ultrathin SnO<sub>x</sub> interlayer via atomic layer deposition (ALD). Due to the passivation effect of the ALD SnO<sub>x</sub> interlayer, carrier recombination at both the intra-grain and grain-boundary regions was suppressed, and Sb interdiffusion from the Sb<sub>2</sub>Se<sub>3</sub> absorber to the cadmium sulfide (CdS) buffer was effectively blocked. Additionally, the rough surface of the co-evaporated Sb<sub>2</sub>Se<sub>3</sub> absorber was mitigated by the conformal deposition of the ALD SnO<sub>x</sub> interlayer, reducing the statistical variation in the photovoltaic parameters of the co-evaporated Sb<sub>2</sub>Se<sub>3</sub> solar cells. The ultrathin ALD SnO<sub>x</sub> interlayer was demonstrated to be a practical strategy for enhancing Sb<sub>2</sub>Se<sub>3</sub> solar cell performance regardless of the absorber's morphology, achieving a substrate-type Sb<sub>2</sub>Se<sub>3</sub> solar cell with an efficiency of 7.395% through the co-evaporation process.

Received 13th March 2025  
Accepted 3rd September 2025

DOI: 10.1039/d5el00031a

rsc.li/EESolar

## Broader context

Low-carbon renewable energy technologies are essential to achieving carbon neutrality. Solar energy, an abundant resource, can replace traditional energy sources. While CuInGaSe<sub>2</sub> (CIGSe) and kesterite Cu<sub>2</sub>ZnSn(S,Se)<sub>4</sub> (CZTSSe) are promising thin-film solar materials, their applications are hindered by the use of rare elements and a large open-circuit voltage deficit. Antimony selenide (Sb<sub>2</sub>Se<sub>3</sub>) has emerged as an alternative due to its 1D crystal structure, high absorption coefficient, and benign grain boundaries. Unlike kesterite, Sb<sub>2</sub>Se<sub>3</sub> offers strong anisotropic charge transport, reducing recombination losses. However, challenges such as interfacial recombination, suboptimal band alignment, and interfacial defects limit its efficiency. To enhance Sb<sub>2</sub>Se<sub>3</sub> solar cell efficiency, researchers focus on interface passivation, doping engineering, and heterojunction optimization. Deposition techniques like close-space sublimation, hydrothermal deposition, and vapor transport deposition have shown promising results. Advancements in defect passivation and band alignment control are crucial for Sb<sub>2</sub>Se<sub>3</sub> to become a commercially viable vacuum thin-film photovoltaic technology, ensuring device uniformity and facilitating large-area fabrication.

## 1. Introduction

Antimony chalcogenides, such as Sb<sub>2</sub>S<sub>3</sub>, Sb<sub>2</sub>Se<sub>3</sub>, and Sb<sub>2</sub>(S,Se)<sub>3</sub>, are well-known compound semiconductors widely used in optoelectronic applications, including photovoltaics, photodetectors, and photoelectrochemical water splitting.<sup>1–3</sup> Due to its unique one-dimensional (1D) crystalline structure, Sb<sub>2</sub>(S,Se)<sub>3</sub> exhibits excellent potential for high-performance photovoltaics, enabling efficient carrier transport along the 1D framework. Various deposition techniques for forming Sb<sub>2</sub>(S,Se)<sub>3</sub> absorber

layers have been reported, including hydrothermal deposition,<sup>4,5</sup> closed-space sublimation,<sup>6–8</sup> vapor transport deposition,<sup>9,10</sup> thermal evaporation,<sup>11,12</sup> rapid thermal evaporation,<sup>13</sup> injection vapor deposition,<sup>14</sup> sputtering with selenization,<sup>15</sup> and chemical bath deposition (CBD).<sup>16</sup> Although hydrothermal and CBD techniques have achieved Sb<sub>2</sub>Se<sub>3</sub> solar cell efficiencies exceeding 10%,<sup>4,16</sup> these solution-based processes pose challenges for large-scale production.

Among various deposition techniques, evaporation has been demonstrated to achieve high efficiency in thin-film solar cells, particularly in Cu(In,Ga)Se<sub>2</sub> (CIGS) devices.<sup>17,18</sup> The co-evaporation process offers several advantages, including a tailored multi-step deposition profile for enhanced efficiency, precise control over the crystalline structure of thin films, elimination of the need for an additional crystallization process, and suitability for large-area deposition. However, in Sb<sub>2</sub>Se<sub>3</sub> solar cell research, the co-evaporation process has yielded relatively lower efficiencies compared to other

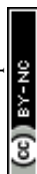
<sup>a</sup>Division of Energy & Environmental Technology, DGIST, Daegu, 42988, Republic of Korea. E-mail: sjsung@dgist.ac.kr; monolith@dgist.ac.kr

<sup>b</sup>Center of Environmental Intelligence, College of Engineering and Computer Science, VinUniversity, Gia Lam District, Hanoi, 14000, Vietnam

<sup>c</sup>Department of Physics, Ewha Womans University, Seoul, 03760, Republic of Korea. E-mail: wmjo@ewha.ac.kr

<sup>d</sup>Department of Interdisciplinary Engineering, DGIST, Daegu, 42988, Republic of Korea

<sup>†</sup> These authors contributed equally to this work.



techniques.<sup>11,12,19–23</sup> Due to the unique 1D crystalline structure of  $\text{Sb}_2\text{Se}_3$ , controlling the morphology of  $\text{Sb}_2\text{Se}_3$  absorbers remains challenging. Additionally, insufficient selenization during the co-evaporation process can degrade absorber quality and promote defect formation.<sup>24,25</sup>

To enhance the photovoltaic performance of solar cell devices, various passivation techniques are commonly employed during device fabrication.<sup>26–28</sup> In particular, due to the relatively poor quality of co-evaporated  $\text{Sb}_2\text{Se}_3$  absorber layers, physical and chemical passivation are essential for achieving high-performance  $\text{Sb}_2\text{Se}_3$  solar cells. Effective passivation of the interface between the  $\text{Sb}_2\text{Se}_3$  absorber and the CdS buffer layer is critical for improving device efficiency. For solar cell passivation, a metal oxide,  $\text{TiO}_2$ , is widely used as a passivation layer due to its wide bandgap and specific electrical properties.<sup>6</sup> Additionally, passivation layers play a crucial role in physically smoothing rough absorber layers.<sup>29</sup> The conformal deposition of passivation layers at interfaces enables the formation of a more uniform cross-sectional structure, which is vital for ensuring device uniformity and facilitating large-area fabrication.

In this study, ultrathin  $\text{SnO}_x$  films deposited *via* atomic layer deposition (ALD) were selected as the interlayer for  $\text{Sb}_2\text{Se}_3$  solar cells. ALD is a well-established technique for fabricating high-quality, ultrathin films.<sup>30–32</sup> Additionally, due to its conformal deposition capability, ALD enables the formation of uniform thin films on various surfaces, regardless of morphology. These unique characteristics make ALD highly suitable for integrating interlayers into  $\text{Sb}_2\text{Se}_3$  solar cells.  $\text{SnO}_x$  is a widely used metal oxide for solar cell passivation due to its wide bandgap, high optical transmittance, superior electron mobility, and chemical stability.<sup>33,34</sup> In this work, the ALD  $\text{SnO}_x$  interlayer was introduced between the  $\text{Sb}_2\text{Se}_3$  absorber and the CdS buffer layer, and its role in device performance was systematically investigated.

An ultrathin ALD  $\text{SnO}_x$  interlayer with a thickness of 2 nm was sufficient to inhibit carrier recombination at the interface between the  $\text{Sb}_2\text{Se}_3$  absorber and the CdS buffer layer. Due to the reduced carrier recombination, the short-circuit current density ( $J_{\text{SC}}$ ) of  $\text{Sb}_2\text{Se}_3$  solar cells incorporating the ALD  $\text{SnO}_x$  interlayer significantly improved. Additionally, the ALD  $\text{SnO}_x$  interlayer served as an effective barrier to elemental diffusion between the  $\text{Sb}_2\text{Se}_3$  absorber and CdS buffer layer. Elemental interdiffusion between the absorber and buffer layer is a known factor contributing to the deterioration of the fill factor (FF) in  $\text{Sb}_2\text{Se}_3$  solar cells.<sup>6,35</sup> In this study, Sb diffusion into the CdS buffer layer was confirmed, and its suppression by the ALD  $\text{SnO}_x$  interlayer was also observed. Consequently,  $\text{Sb}_2\text{Se}_3$  solar cells with the ALD  $\text{SnO}_x$  interlayer exhibited a pronounced enhancement in FF compared to devices without the interlayer.

In addition to its barrier effect, the ALD  $\text{SnO}_x$  interlayer was found to compensate for the relatively rough surface of co-evaporated  $\text{Sb}_2\text{Se}_3$  absorbers through uniform and conformal deposition. This morphological passivation effect improved the overall device structure, leading to a narrower distribution of photovoltaic parameters in  $\text{Sb}_2\text{Se}_3$  solar cells. Furthermore, the impact of the ALD  $\text{SnO}_x$  interlayer on charge distribution at

grain boundaries in  $\text{Sb}_2\text{Se}_3$  solar cells was observed. The introduction of the ALD  $\text{SnO}_x$  interlayer weakened band bending at CdS grain boundaries and significantly reduced potential variations. This altered potential profile effectively inhibited carrier recombination at grain boundaries, further enhancing device performance.

The investigation of the ALD  $\text{SnO}_x$  interlayer in  $\text{Sb}_2\text{Se}_3$  solar cells demonstrated its effectiveness as a passivation strategy for co-evaporated  $\text{Sb}_2\text{Se}_3$  solar cells, regardless of absorber morphology.  $\text{Sb}_2\text{Se}_3$  solar cells incorporating the ALD  $\text{SnO}_x$  interlayer achieved an efficiency of 7.395%, the highest reported for co-evaporated  $\text{Sb}_2\text{Se}_3$  solar cells. Further optimization of the ALD  $\text{SnO}_x$  interlayer has the potential to further enhance device performance.

## 2. Results and discussion

### 2.1 Characteristics of thin $\text{MoSe}_2$ -based devices with a passivation layer

Interfacial engineering at the absorber/buffer interface in  $\text{Sb}_2\text{Se}_3$ -based substrate-configuration solar cells has been extensively studied, particularly with the application of CdZnS or  $\text{In}_2\text{Se}_3$  to modify energy band alignment and analyze their effects on surface chemistry.<sup>36,37</sup> However, no studies have yet reported the use of an  $\text{SnO}_x$  layer in substrate-configured cells for absorber surface passivation, though such advancements are expected as the technology continues to develop. In this study, the substrate configuration of  $\text{Sb}_2\text{Se}_3$  thin-film solar cells was investigated, utilizing the co-evaporation method to enhance efficiency. The source-to-substrate distance was set at 50 cm to ensure a smooth  $\text{Sb}_2\text{Se}_3$  film and prevent overheating. A detailed schematic of the co-evaporation process is presented in Fig. S1 (SI). The low efficiency of co-evaporated  $\text{Sb}_2\text{Se}_3$  has primarily been attributed to challenges in fabricating high-quality absorbers in a high-vacuum chamber and the difficulty of controlling pyro-temperatures.

To evaluate the effect of the ALD  $\text{SnO}_x$  interlayer on device performance,  $\text{Sb}_2\text{Se}_3$  solar cells were fabricated with a substrate configuration of  $\text{Mo}/\text{MoSe}_2/\text{Sb}_2\text{Se}_3/\text{SnO}_x/\text{CdS}/\text{i-ZnO}/\text{AZO}/\text{Al}$ . The statistical distributions of power conversion efficiency (PCE), open-circuit voltage ( $V_{\text{OC}}$ ), short-circuit current density ( $J_{\text{SC}}$ ), and fill factor (FF) for devices with and without the ALD  $\text{SnO}_x$  interlayer are presented in Fig. 1a–d. The results demonstrated that the ALD  $\text{SnO}_x$  interlayer effectively enhanced the efficiency of  $\text{Sb}_2\text{Se}_3$  solar cells. Additionally, co-evaporated  $\text{Sb}_2\text{Se}_3$  solar cells with  $\text{SnO}_x$  exhibited a narrower distribution of photovoltaic parameters, likely due to the reduced roughness of the  $\text{Sb}_2\text{Se}_3/\text{CdS}$  interface facilitated by the ALD  $\text{SnO}_x$  interlayer. The current density–voltage ( $J$ – $V$ ) curves of the best-performing devices are shown in Fig. 1e, with the corresponding photovoltaic parameters listed in Table 1. The  $\text{Sb}_2\text{Se}_3$  solar cell without the ALD  $\text{SnO}_x$  interlayer achieved a maximum PCE of 3.998%, with a  $V_{\text{OC}}$  of 0.478 V, a  $J_{\text{SC}}$  of  $22.075 \text{ mA cm}^{-2}$ , and an FF of 37.836%. Notably, the  $\text{Sb}_2\text{Se}_3$  device incorporating the ALD  $\text{SnO}_x$  interlayer achieved an enhanced PCE of 6.250%, with a  $V_{\text{OC}}$  of 0.434 V,  $J_{\text{SC}}$  of  $28.007 \text{ mA cm}^{-2}$ , and an FF of 51.421%. Among these parameters,  $J_{\text{SC}}$  and FF exhibited a significant



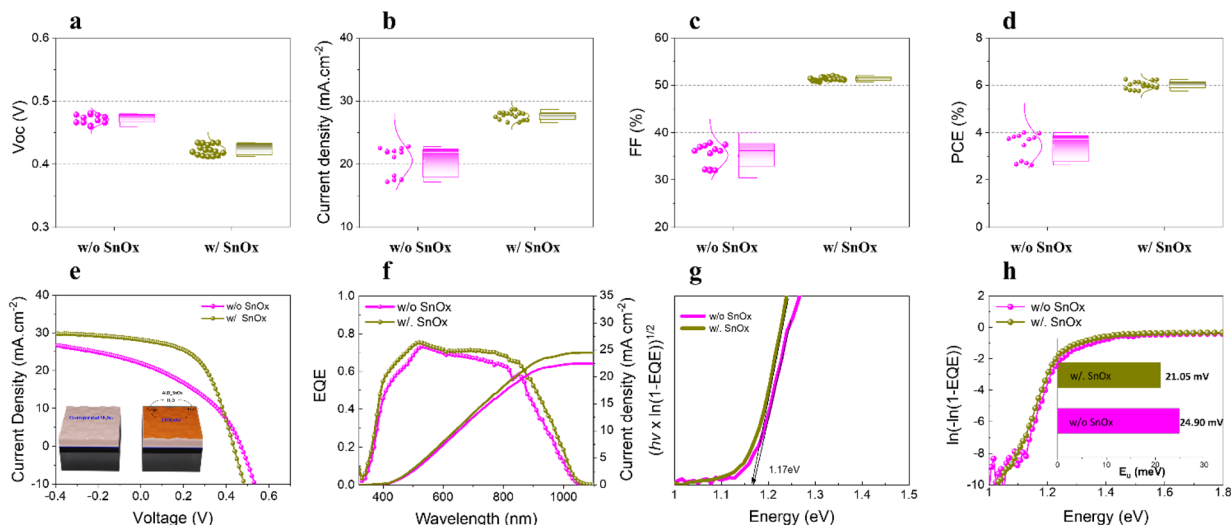


**Fig. 1** (a–d) Box plots of solar cell parameters for the tested devices. (e) Current density–voltage ( $J$ – $V$ ) curves of the highest-efficiency device within each group. (f) EQE spectrum of the best-performing device based on the standard AM 1.5G solar spectrum. (g) The bandgap calculated from EQE spectra. (h) Urbach energy values derived from EQE spectra for the control-Sb<sub>2</sub>Se<sub>3</sub> and SnO<sub>x</sub>–Sb<sub>2</sub>Se<sub>3</sub> solar cells, respectively.

increase due to the non-ohmic space-charge-limited current, which contributed to the nonlinear shunt current in Sb<sub>2</sub>Se<sub>3</sub> thin-film solar cells. The highly resistive transparent SnO<sub>x</sub> layer functioned as a buffer between the CdS window layer, mitigating the formation of shunt paths at the CdS/Sb<sub>2</sub>Se<sub>3</sub> interface.<sup>38</sup> This improvement can be attributed to the passivation and protection of the Sb<sub>2</sub>Se<sub>3</sub> absorber layer, which reduced recombination losses and enhanced carrier transport within the device. These findings demonstrate the effectiveness of the ALD SnO<sub>x</sub> interlayer in improving the efficiency of co-evaporated Sb<sub>2</sub>Se<sub>3</sub> solar cells.

The external quantum efficiency (EQE) data in Fig. 1f indicate that both devices exhibited a photoelectronic response from 300 to 1100 nm, with the bandgap of Sb<sub>2</sub>Se<sub>3</sub> devices—with and without the ALD SnO<sub>x</sub> interlayer. Notably, the two EQE curves displayed identical onset wavelengths, suggesting that both cases of Sb<sub>2</sub>Se<sub>3</sub> absorbers had equivalent bandgaps. Previous studies have demonstrated that introducing a high-resistivity SnO<sub>2</sub> layer *via* pulsed laser deposition in the superstrate configuration reduces reflection at the front electrode and enhances carrier collection efficiency.<sup>39</sup> Therefore, the Sb<sub>2</sub>Se<sub>3</sub> device with the ALD SnO<sub>x</sub> interlayer exhibited increased EQE in the long-wavelength region (600–1100 nm). We observed that

the integrated current densities derived from the EQE curves were 22.45 and 24.49 mA cm<sup>−2</sup> for the control and modified devices, respectively. These values were lower than the  $J_{SC}$  measured from the corresponding  $J$ – $V$  curves. This discrepancy in  $J_{SC}$  between the EQE and  $J$ – $V$  curves has also been reported in previous studies on Sb<sub>2</sub>Se<sub>3</sub> solar cells, which can be attributed to the deep levels in the junction region.<sup>16,40</sup> The photogenerated carriers can recombine at these centers at low light levels (EQE measurement), whereas some of these centers are more likely to be occupied due to photoexcitation in high light intensity (under AM 1.5G illumination at 100 mW cm<sup>−2</sup>).

The indirect bandgaps of devices without and with the SnO<sub>x</sub> interlayer were determined to be 1.17 eV, by extrapolating the linear region of the  $(h\nu \times \ln(1 - EQE))^{1/2}$  versus  $h\nu$  plots to the horizontal photon energy axis (Fig. 1g).<sup>41</sup> The observed bandgap variation was consistent with the chemical composition, as a higher Se content in the co-evaporated Sb<sub>2</sub>Se<sub>3</sub> thin film resulted in a lower bandgap value, consistent with our density functional theory (DFT) calculations in the recent discovery.<sup>42</sup> The ALD SnO<sub>x</sub> interlayer likely functioned as an efficient electron transport channel between the Sb<sub>2</sub>Se<sub>3</sub> absorber and CdS buffer layers, helping electron movement across the Sb<sub>2</sub>Se<sub>3</sub>/CdS junction. Urbach energy ( $E_U$ ), a metric used to quantify the

**Table 1** Photovoltaic parameters of co-evaporated Sb<sub>2</sub>Se<sub>3</sub> solar cells with and without the ALD SnO<sub>x</sub> interlayer, measured under AM 1.5G illumination

Samples		$V_{OC}$ (V)	$J_{SC}$ (mA cm <sup>−2</sup> )	FF (%)	PCE (%)	$E_g$ (eV)	$E_A$ (eV)	$E_A/E_g$ (%)	$G$ (mS cm <sup>−2</sup> )	$R$ (Ω cm <sup>2</sup> )	$A$	$J_0$ (mA cm <sup>−2</sup> )
W/o SnO <sub>x</sub>	Average	0.470	20.872	35.468	3.500							
	StDev	0.008	2.157	2.254	0.529							
	Champion	0.478	22.075	37.836	3.998	1.17	1.00	85.47	18.58	0.26	6.10	0.638
w/SnO <sub>x</sub>	Average	0.422	27.553	50.911	5.926							
	StDev	0.006	0.657	0.561	0.169							
	Champion	0.434	28.007	51.421	6.250	1.17	1.04	88.89	7.30	2.43	2.08	0.027



extent of the band tail effect, was derived from the  $\ln(1 - EQE)$  versus energy curve, as shown in Fig. 1h. Upon incorporating the ALD  $\text{SnO}_x$  interlayer,  $E_U$  significantly decreased from 24.90 meV to 21.05 meV, suggesting that recombination near the  $\text{Sb}_2\text{Se}_3/\text{CdS}$  junction was mitigated due to the passivation of detrimental defects, a topic further discussed in later sections.

The fabrication techniques for co-evaporated  $\text{Sb}_2\text{Se}_3$  thin-film solar cells are illustrated in Fig. 2a and described in the "Experimental" section. The surface and cross-sectional morphologies of the as-prepared films were analyzed using scanning electron microscopy (SEM), revealing an estimated  $\text{Sb}_2\text{Se}_3$  grain size of approximately 290 nm. Fig. 2b–g present top-view SEM images of the co-evaporated  $\text{Sb}_2\text{Se}_3$  absorbers and CdS buffer layers deposited on  $\text{Sb}_2\text{Se}_3$ , as well as cross-sectional SEM images of the co-evaporated  $\text{Sb}_2\text{Se}_3$  devices with and without the 2 nm ALD  $\text{SnO}_x$  interlayer. The SEM images reveal a compact and uniform CdS grain coverage with no visible pinholes between the grains and strong adhesion to the  $\text{Sb}_2\text{Se}_3$  absorber surface. However, the surface roughness is expected to be high, with wide grain boundaries clear in the surface SEM images. These deep, valley-like grain boundaries could hinder uniform CdS formation. The application of an ALD  $\text{SnO}_x$

interlayer may mitigate this issue by improving coverage and promoting more uniform CdS growth in these regions. Notably, CdS buffer layer morphology undergoes significant changes with increasing ALD  $\text{SnO}_x$  interlayer thickness from 0 to 5 nm, as evidenced by the SEM images in Fig. S2, SI.  $\text{SnO}_x$  is expected to play a crucial role in bridging narrow and deep features that the CdS layer struggles to cover uniformly. However, our findings indicate that CdS exhibits inferior growth on the oxide surface compared to the chalcogenide surface. Increasing the thickness of the ALD  $\text{SnO}_x$  interlayer altered the morphology of the CdS buffer layers, leading to the formation of discrete nanoparticles. Therefore, to ensure consistent CdS coverage, the  $\text{SnO}_x$  layer was constrained to an optimal thickness of 2 nm. Furthermore, device performance was highly dependent on the ALD  $\text{SnO}_x$  interlayer thickness. Notably, only ultrathin ALD  $\text{SnO}_x$  interlayers enhanced performance, with an optimal thickness of 2 nm, while thicker interlayers (>2 nm) resulted in a decline in  $V_{OC}$  (Fig. S3, SI and Table S1).

The crystal structure and phase purity of the co-evaporated  $\text{Sb}_2\text{Se}_3$  thin film were analyzed using X-ray diffraction (XRD), as shown in Fig. 3a. The  $\text{Sb}_2\text{Se}_3$  exhibited an orthorhombic crystal structure, classified under the space group Pbnm (JCPDS

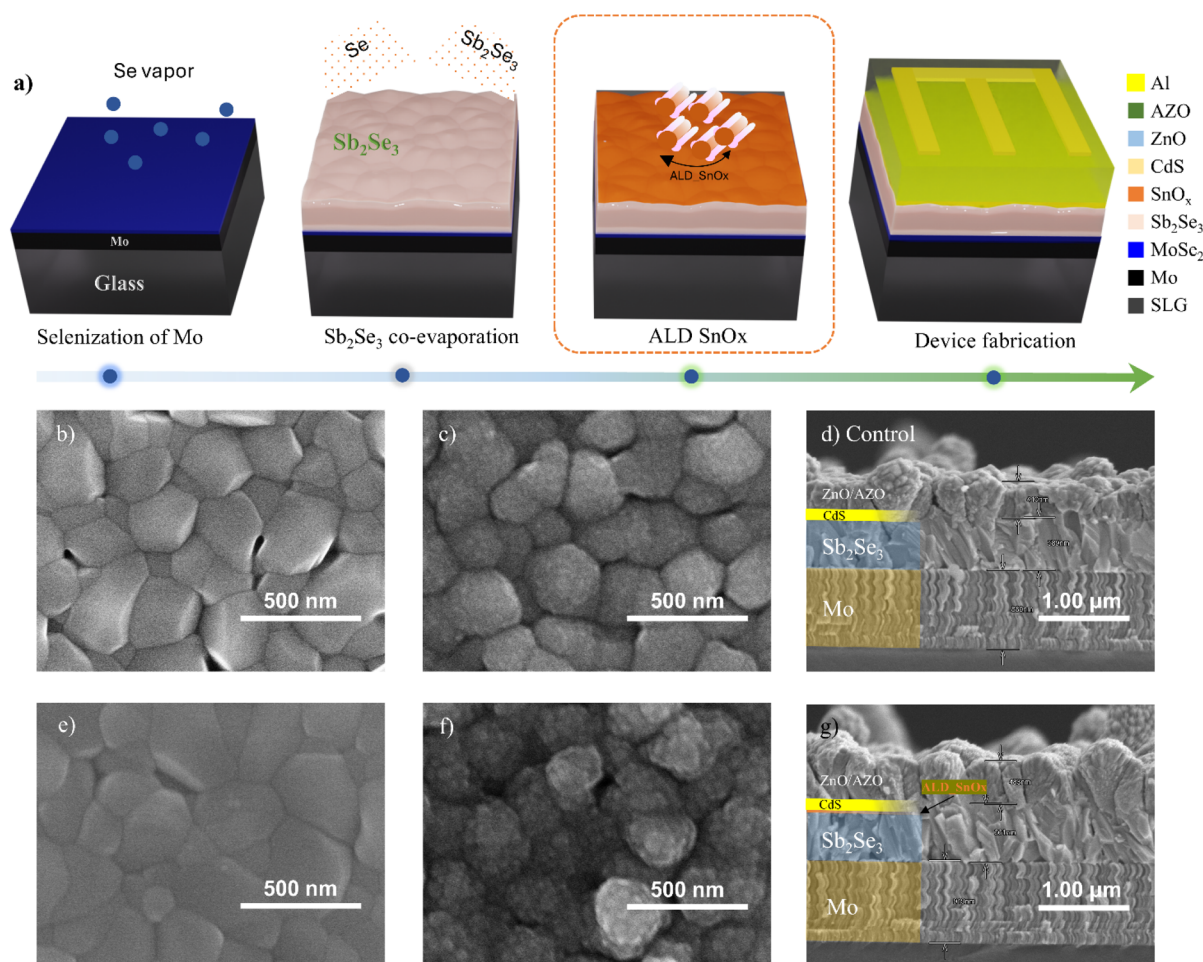
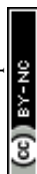


Fig. 2 (a) Schematic representation of the fabrication process for co-evaporated  $\text{Sb}_2\text{Se}_3$  solar cells with glass/Mo/MoSe<sub>2</sub>/Sb<sub>2</sub>Se<sub>3</sub>/SnO<sub>x</sub>/CdS/ZnO/AZO/Al architecture. (b–d) Top-view SEM images of the  $\text{Sb}_2\text{Se}_3$  layer, CdS/ $\text{Sb}_2\text{Se}_3$  layer, and cross-sectional SEM images of devices without the ALD  $\text{SnO}_x$  interlayer. (e–g) Corresponding SEM images of devices incorporating the ALD  $\text{SnO}_x$  interlayer.



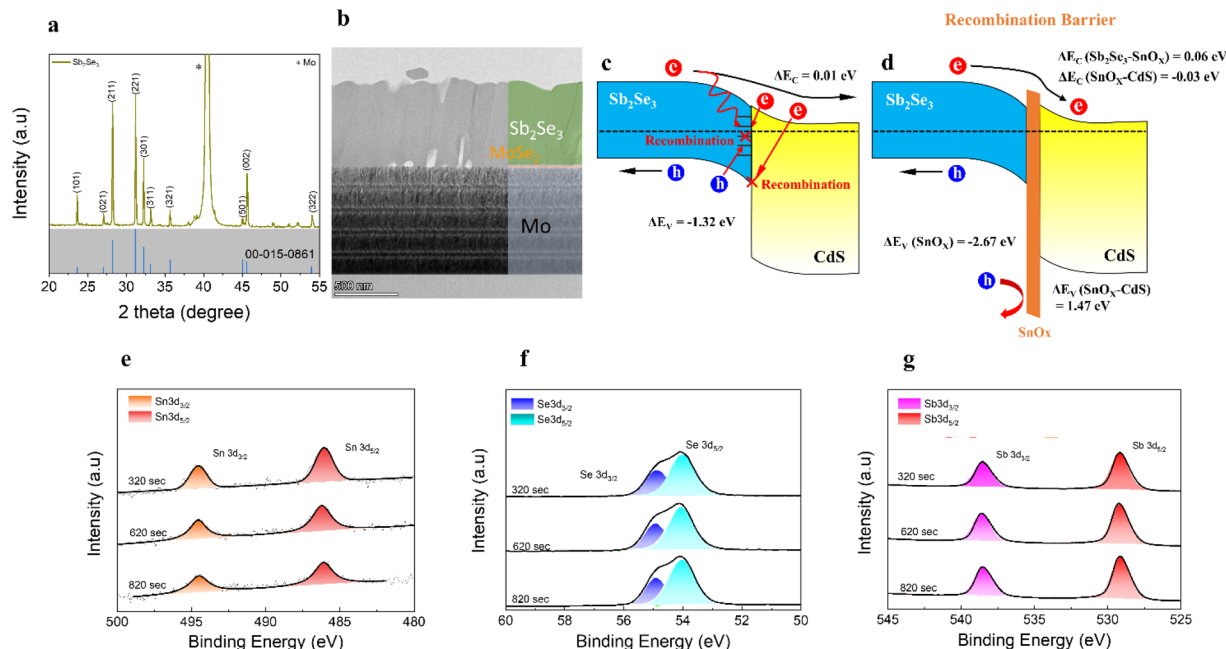


Fig. 3 (a) XRD pattern and (b) HRTEM image of the co-evaporated  $\text{Sb}_2\text{Se}_3$  absorber on the  $\text{MoSe}_2/\text{Mo}$  substrate. (c and d) Energy band structure of the  $\text{Sb}_2\text{Se}_3$  absorber and CdS buffer without and with the ALD  $\text{SnO}_x$  interlayer, respectively. (e–g) X-ray photoelectron spectroscopy (XPS) spectra of the co-evaporated  $\text{Sb}_2\text{Se}_3$  absorber covered with the ALD  $\text{SnO}_x$  interlayer at various etching depths (320–820 s).

00-015-0861), with no detectable impurity phases. Notably, only strong ( $hkl$ ) diffraction peaks were observed in the XRD pattern, indicating a preferred orientation along the  $c$ -axis. The intensity ratios  $I_{011}/I_{221}$  and  $I_{002}/I_{221}$  were 0.13 and 0.34, respectively, confirming the (221)-preferred orientation of the co-evaporated  $\text{Sb}_2\text{Se}_3$  thin film. To quantify differences in crystalline orientations, the texture coefficient (TC) of the diffraction peaks was

calculated using the equation:  $\text{TC}_{hkl} = \frac{I_{(hkl)}}{I_{0(hkl)}} / \left( \frac{1}{N} \sum_N \frac{I_{(hkl)}}{I_{0(hkl)}} \right)$ ,

where  $I_{(hkl)}$  represents the observed peak intensity of the ( $hkl$ ) plane,  $I_{0(hkl)}$  is the corresponding standard XRD intensity, and  $N$  is the total number of reflections considered for the calculation.<sup>43</sup> A higher TC value for a given diffraction peak indicates a stronger preferred orientation along that direction. As shown in Fig. S4, SI, the co-evaporated  $\text{Sb}_2\text{Se}_3$  thin film deposited at 315 °C exhibited a ( $hkl$ ) preferred orientation, particularly along (221) and (211). The cross-sectional high-resolution transmission electron microscopy (HRTEM) image revealed a flat and uniform morphology of the co-evaporated  $\text{Sb}_2\text{Se}_3$  thin film (Fig. 3b). Additionally, the interplanar  $d$ -spacing of 0.523 nm corresponded to the (210) planes of orthorhombic  $\text{Sb}_2\text{Se}_3$ , as shown in Fig. S5, SI. This value was consistent with the  $d$ -spacing observed in one-dimensional (1D) single-crystalline  $\text{Sb}_2\text{Se}_3$  nanostructures synthesized by other methods.<sup>6,44,45</sup>

The application of an ALD  $\text{SnO}_x$  interlayer on the  $\text{Sb}_2\text{Se}_3$  absorber *via* ALD was found to improve  $J_{\text{SC}}$ , FF, and overall power conversion efficiency. To better understand this improvement, an energy band diagram was constructed based on ultraviolet photoelectron spectroscopy (UPS) analysis, comparing the  $\text{Sb}_2\text{Se}_3/\text{CdS}$  and  $\text{Sb}_2\text{Se}_3/\text{SnO}_x/\text{CdS}$  heterojunctions. The results revealed that the  $\text{Sb}_2\text{Se}_3/\text{CdS}$  interface

exhibited a weak spike-like conduction band offset (CBO) of  $\Delta E_{\text{C}} = 0.01$  eV, whereas the introduction of the ALD  $\text{SnO}_x$  interlayer led to a more pronounced spike CBO of  $\Delta E_{\text{C}}(\text{Sb}_2\text{Se}_3\text{-SnO}_x) = 0.06$  eV in the  $\text{Sb}_2\text{Se}_3/\text{SnO}_x/\text{CdS}$  structure. The increased spike CBO effectively suppresses the backflow of electrons, reducing interfacial carrier recombination. In the  $\text{Sb}_2\text{Se}_3/\text{CdS}$  heterojunction, the low CBO allowed electrons to transfer easily into CdS; however, it also increased the possibilities of electron backflow and recombination. In contrast, with the  $\text{SnO}_x$  interlayer, the higher spike CBO restricts electron backflow while maintaining efficient electron transport toward CdS, leading to improved charge transport and increased  $J_{\text{SC}}$ . However, an excessively large spike CBO can also increase transport resistance, impeding electron injection. This effect can result in charge accumulation, enhanced interfacial recombination, and a reduction in the  $V_{\text{OC}}$ . As the CBO increases with the insertion of  $\text{SnO}_x$ , an additional energy barrier is formed at the interface, potentially slowing electron transport. Therefore, in spike-type band alignment, it is crucial to balance electron backflow suppression and forward transport resistance minimization. Experimental results indicate that increasing the  $\text{SnO}_x$  thickness correlates with a reduction in  $V_{\text{OC}}$  (Fig. S3, SI). Thus, for optimal device performance, fine-tuning the  $\text{SnO}_x$  thickness is expected to be an effective strategy for preventing  $V_{\text{OC}}$  degradation while maintaining  $J_{\text{SC}}$  improvement. Additionally, the insertion of  $\text{SnO}_x$  significantly affects the valence band offset (VBO), enhancing the hole-blocking effect. The  $\text{Sb}_2\text{Se}_3/\text{SnO}_x$  interface exhibited a substantial increase in VBO to  $-2.67$  eV, effectively preventing hole backflow and reducing hole recombination at the interface (Fig. S6, SI). This strengthened VBO contributes to an increase in  $J_{\text{SC}}$  and FF, further enhancing

device efficiency. As a result, introducing an ALD  $\text{SnO}_x$  interlayer improves device performance by forming a spike CBO that effectively blocks electron backflow and enhances  $J_{\text{SC}}$ . However, an excessive CBO increase can lead to higher transport resistance and a subsequent decrease in  $V_{\text{OC}}$ . To mitigate this, further optimization of the CBO and precise thickness control of  $\text{SnO}_x$  are necessary. Furthermore, the increased VBO resulting from  $\text{SnO}_x$  insertion strengthens hole blocking, reducing recombination and positively impacting  $J_{\text{SC}}$  and FF. These findings demonstrate that  $\text{SnO}_x$  incorporation is an effective strategy for improving  $\text{Sb}_2\text{Se}_3$ -based solar cell performance, highlighting the need for further design refinements to achieve optimal efficiency.

The XPS results at various etching depths (Fig. 3e–g) further support the penetration of  $\text{SnO}_x$  into the  $\text{Sb}_2\text{Se}_3$  absorber. The presence of Sn within the vacant regions of the  $\text{Sb}_2\text{Se}_3$  layer, facilitated by the exceptional coverage of ALD  $\text{SnO}_x$ , indicates that  $\text{SnO}_x$  effectively passivated the entire  $\text{Sb}_2\text{Se}_3$  layer, reducing the probability of shunt path formation. Fig. 3e presents the Sn content within the  $\text{Sb}_2\text{Se}_3$  absorber at etching depths ranging from 320 s to 820 s. As the etching depth increased, the Sn ion content gradually decreased until reaching the Mo substrate, with the total  $\text{Sb}_2\text{Se}_3$  thickness estimated at approximately 700 nm. Notably, Sn signals remained detectable even after prolonged etching, providing evidence of the deep penetration achieved by the ALD process, consistent with TEM and SEM analyses. Additionally, the presence of various surface nanorods may have contributed to Sn signal detection during depth profiling, further reinforcing the effectiveness of the coverage. The two peaks at 54.6 and 53.7 eV (Fig. 3f) correspond to  $\text{Se } 3d_{3/2}$  and  $\text{Se } 3d_{5/2}$  of  $\text{Sb}_2\text{Se}_3$ , respectively. Similarly, Fig. 3g shows peaks centered at high binding energies of 538.7 and 529.7 eV, attributed to  $\text{Sb } 3d_{3/2}$  and  $\text{Sb } 3d_{5/2}$  of  $\text{Sb}_2\text{Se}_3$ .<sup>20,46,47</sup> Moreover, the XPS spectra of CdS buffers on  $\text{Sb}_2\text{Se}_3$  and  $\text{Sb}_2\text{Se}_3/\text{SnO}_x$  exhibited no significant peak shifts or the appearance of Cd and S after a 10 s etching time (Fig. S7, SI).

The ALD  $\text{SnO}_x$  interlayer would likely affect charge transport between  $\text{Sb}_2\text{Se}_3$  and CdS, potentially resulting in an alteration of the electrical potential distribution. The Kelvin probe force microscopy (KPFM) method was employed to investigate

potential variations within the CdS layer by measuring surface potential distribution. The topography and local potential mapping results obtained on the CdS surface with and without  $\text{SnO}_x$  are presented in Fig. 4a. The histogram of contact potential distribution ( $V_{\text{CPD}}$ ) was extracted from the mapping data (Fig. 4b). With the introduction of the ALD  $\text{SnO}_x$  interlayer, the FWHM of the  $V_{\text{CPD}}$  distribution decreased from 26 mV to 21.5 mV, showing the formation of a homogeneous potential distribution in the CdS buffer layer. The band bending arising from the irregular potential distribution could exert a force on electrons, the major charge carriers in the CdS layer. Therefore, without the  $\text{SnO}_x$  layer, localized forces induced near the GBs could generate lateral electron flow, potentially disrupting carrier transport toward the TCO layer.<sup>48</sup> Based on the results, the role of the ALD  $\text{SnO}_x$  interlayer could be suggested as a capping layer, producing more uniform contact between the absorber and buffer layers by mitigating band bending at GBs.<sup>49</sup> This consequently enables the formation of a more homogeneous and broader p–n junction area, enhancing electron transport across the interface.

To further prove the enhanced charge transport facilitated by the ALD  $\text{SnO}_x$  interlayer, the band structure of CdS was examined in relation to the presence of  $\text{SnO}_x$ . We suggest an energy band alignment, as shown in Fig. 4c and Fig. S8, SI, constructed based on ultraviolet-visible (UV-vis) and ultraviolet photoelectron spectroscopy (UPS) measurements. The bandgap of CdS, calculated from UV-vis spectra, was determined to be 2.4 eV for both samples with and without  $\text{SnO}_x$ . A reduction in the energy difference between  $E_{\text{CBM}}$  and  $E_{\text{F}}$  ( $|E_{\text{CBM}} - E_{\text{F}}|$ ) of 50 meV was observed in the CdS with  $\text{SnO}_x$  compared to CdS without  $\text{SnO}_x$ . The shift of the Fermi level toward the conduction band minimum (CBM) indicates an increase in electron concentration with the introduction of  $\text{SnO}_x$ .<sup>50</sup> This confirms improved charge separation at the junction between the  $\text{Sb}_2\text{Se}_3$  and CdS layers, consistent with the KPFM results. Moreover, a decrease in the work function of 300 meV was observed in CdS with  $\text{SnO}_x$ . The modified energy band alignment is energetically favorable, inducing a strong built-in potential at the CdS/TCO interface under short-circuit conditions.<sup>51</sup> This configuration can facilitate carrier extraction and contribute to  $J_{\text{SC}}$  enhancement.<sup>52</sup>

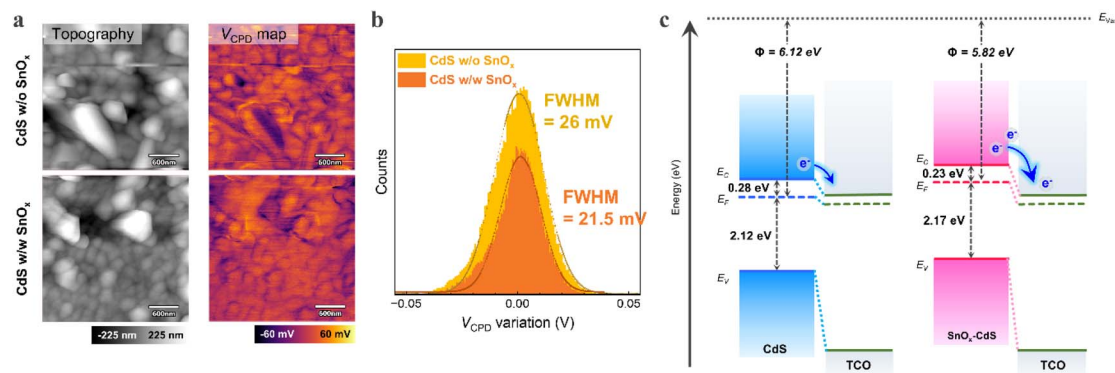


Fig. 4 (a) KPFM images of the CdS buffer layer and (b) histogram of the potential distribution of the CdS surface with or without the ALD  $\text{SnO}_x$  interlayer and (c) band structure diagram of CdS and  $\text{SnO}_x$  from UPS measurements.



## 2.2 Interdiffusion at the absorber–buffer interface

To examine the effect of the ALD  $\text{SnO}_x$  interlayer on the microstructure of co-evaporated  $\text{Sb}_2\text{Se}_3$  solar cells, various analytical techniques were employed. High-resolution TEM images of the devices (Fig. S9, SI) provide detailed insights into the microstructural evolution and interfacial characteristics, particularly at the  $\text{CdS}/\text{Sb}_2\text{Se}_3$  and  $\text{Mo}/\text{MoSe}_2/\text{Sb}_2\text{Se}_3$  interface regions. The introduction of the ALD  $\text{SnO}_x$  interlayer improved the  $\text{Sb}_2\text{Se}_3$  device structure, yielding a smoother interface and enhancing the adhesion between the  $\text{Sb}_2\text{Se}_3$  and  $\text{CdS}$  layers. For a more precise microstructural analysis, high-angle annular dark-field (HAADF) imaging and energy-dispersive X-ray spectroscopy (EDS) elemental mapping were performed. Fig. S10 and S11, SI present the HAADF images and EDS elemental maps of the  $\text{Sb}_2\text{Se}_3/\text{CdS}$  interfacial region, both with and without the ALD  $\text{SnO}_x$  interlayer. In both cases, Sb and Se elements exhibited uniform distribution throughout the  $\text{Sb}_2\text{Se}_3$  absorber layer, confirming the homogeneous composition of the material. However, HAADF images of each  $\text{Sb}_2\text{Se}_3$  device revealed

differences in the distribution of layers. The  $\text{Sb}_2\text{Se}_3$  device with the ALD  $\text{SnO}_x$  interlayer exhibited improved uniformity of the  $\text{CdS}$  buffer and AZO transparent conducting oxide (TCO), likely due to morphological changes in the  $\text{CdS}$  buffer on the ALD  $\text{SnO}_x$  interlayer. Additionally, EDS elemental composition maps showed no thermally induced interdiffusion, showing that the co-evaporated  $\text{Sb}_2\text{Se}_3$  absorber and  $\text{CdS}$  buffer remained free of cross-contamination during the chemical bath deposition (CBD) process of the  $\text{CdS}$  buffer layer. The EDX line scan further confirmed the absence of thermal diffusion in the heterojunction.

To precisely examine the coverage of the  $\text{CdS}$  buffer layer on the  $\text{Sb}_2\text{Se}_3$  absorber and the interdiffusion of elements at the  $\text{CdS}/\text{Sb}_2\text{Se}_3$  interface, HRTEM-EDS analysis was performed. As shown in Fig. 5a–c, spatial elemental mapping of Sb revealed variations in color intensity, indicating notable interfacial interdiffusion of Sb into the  $\text{CdS}$  buffer layer, whereas no significant interdiffusion of Se was observed (Fig. S12, SI). The presence of Sb in the  $\text{CdS}$  buffer layer likely resulted from the

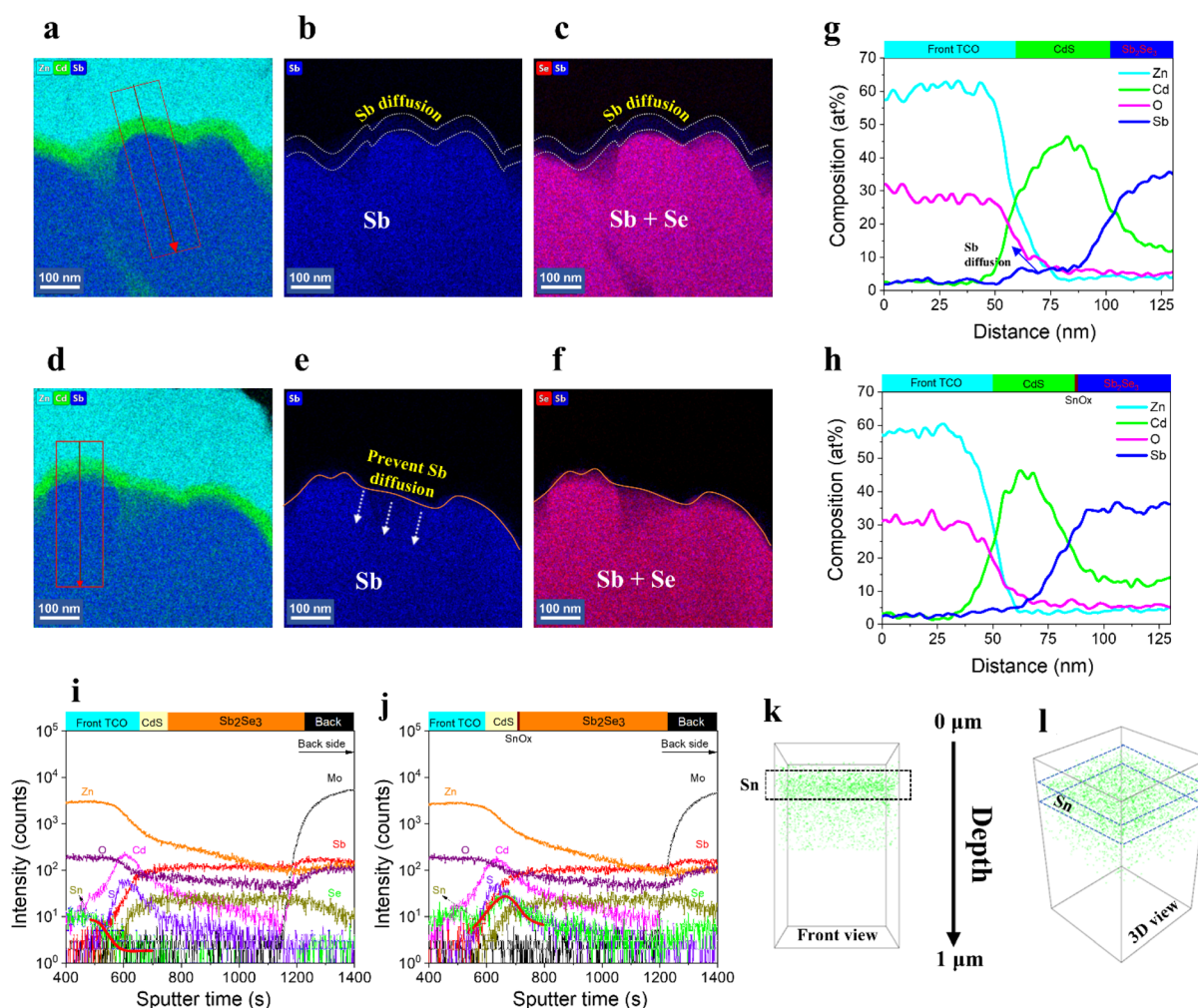
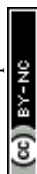


Fig. 5 HRTEM-EDS images of  $\text{Sb}_2\text{Se}_3$  devices (a–c) without an ALD  $\text{SnO}_x$  interlayer and (d–f) with an ALD  $\text{SnO}_x$  interlayer. EDX line scans of Zn, Cd, O and Sb across (g) the TCO/ $\text{CdS}/\text{Sb}_2\text{Se}_3$  interface and (h) the TCO/ $\text{CdS}/\text{SnO}_x/\text{Sb}_2\text{Se}_3$  interface. TOF-SIMS depth profile showing elemental mapping of devices (i) without an ALD  $\text{SnO}_x$  interlayer and (j) with an ALD  $\text{SnO}_x$  interlayer. TOF-SIMS 3D tomography of the Sn element: (k) front view and (l) 3D view focusing on the  $\text{Sb}_2\text{Se}_3/\text{SnO}_x$  interlayer.



dissolution of  $\text{Sb}_2\text{Se}_3$  in the alkaline ammonia solution, leading to its reaction with  $\text{NH}_4^+$  during the CBD process.<sup>6,53–55</sup> However, Sb interdiffusion was mitigated by the ALD  $\text{SnO}_x$  interlayer, which blocked direct contact between  $\text{Sb}_2\text{Se}_3$  and  $\text{NH}_4^+$  at the  $\text{Sb}_2\text{Se}_3/\text{CdS}$  interface (Fig. 5d–f). EDS line scans of Zn, Cd, O, and Sb across the interfaces are presented in Fig. 5g, h. The line scans show a small step increase in Sb over a distance of 30–35 nm in the CdS layer of the control sample, as confirmed by the slight accumulation of Sb at the highest intensity of the Cd signal before a significant increase in the Sb signal. In contrast, no step-function increase was observed for the  $\text{SnO}_x$ -based device, convincingly suggesting that the  $\text{SnO}_x$  layer is effective in reducing or preventing the diffusion of Sb into the CdS layer or near the  $\text{Sb}_2\text{Se}_3/\text{CdS}$  interlayer.

To verify the presence and interdiffusion of Sb at the  $\text{Sb}_2\text{Se}_3$  device interface, time-of-flight secondary ion mass spectrometry (TOF-SIMS) depth profiling was performed on  $\text{Sb}_2\text{Se}_3$  devices with and without the ALD  $\text{SnO}_x$  interlayer (Fig. 5i and j). In the presence of the ALD  $\text{SnO}_x$  interlayer, an intense Sn ion signal was detected at the interface between the  $\text{Sb}_2\text{Se}_3$  absorber and CdS buffer. However, no significant difference in Sb ion concentration was observed due to the low interdiffusion level. These results align with the widespread diffusion pattern identified in the 3D tomography analysis of Sn ions, which were predominantly detected at the  $\text{Sb}_2\text{Se}_3/\text{CdS}$  junction along with the absorber thickness (Fig. 5k and l). The TOF-SIMS 3D

tomography results for different elements in  $\text{Sb}_2\text{Se}_3$  devices are shown in Fig. S13, SI. The 3D-rendered overlay of elements further clarifies the position of each component, confirming that Sn ions are incorporated into the  $\text{Sb}_2\text{Se}_3$  absorber region.

### 2.3 Carrier transport dynamics and defect characterization

The  $J$ - $V$  curves of the solar cells (Fig. 6a) clearly demonstrate the significant impact of the ALD  $\text{SnO}_x$  interlayer on the photovoltaic performance of co-evaporated  $\text{Sb}_2\text{Se}_3$  solar cells. The  $\text{Sb}_2\text{Se}_3$  device without the  $\text{SnO}_x$  interlayer exhibited lower power conversion efficiency (PCE), whereas the device with the ALD  $\text{SnO}_x$  interlayer achieved a higher PCE. The saturation current density and diode ideality factor were extracted using the single-diode equation:  $\ln(J + J_{\text{sc}} - GV) = \ln(J_0) + \left(\frac{q}{AkT}\right)(V - R_s J)$ , where  $J_0$ ,  $G$ ,  $V$ ,  $q$ ,  $A$ ,  $k$ ,  $T$ , and  $R_s$  represent the saturation current density, shunt conductance, voltage, electron charge, diode ideality factor, Boltzmann's constant, temperature, and series resistance, respectively.<sup>53</sup> Notably, significant differences were primarily observed in the fill factor (FF) and short-circuit current density ( $J_{\text{sc}}$ ) by analyzing the values of  $A$  and  $J_0$  obtained from fitting the  $\ln(J + J_{\text{sc}} - GV)$  versus  $(V - R_s J)$  curves. Specifically,  $dV/dJ$  versus  $(J + J_{\text{sc}})^{-1}$  and  $dJ/dV$  versus voltage ( $V$ ) plots (Fig. 6b and c) were used to evaluate the series resistance and average shunt conductance, respectively. Notably, deep defects at grain

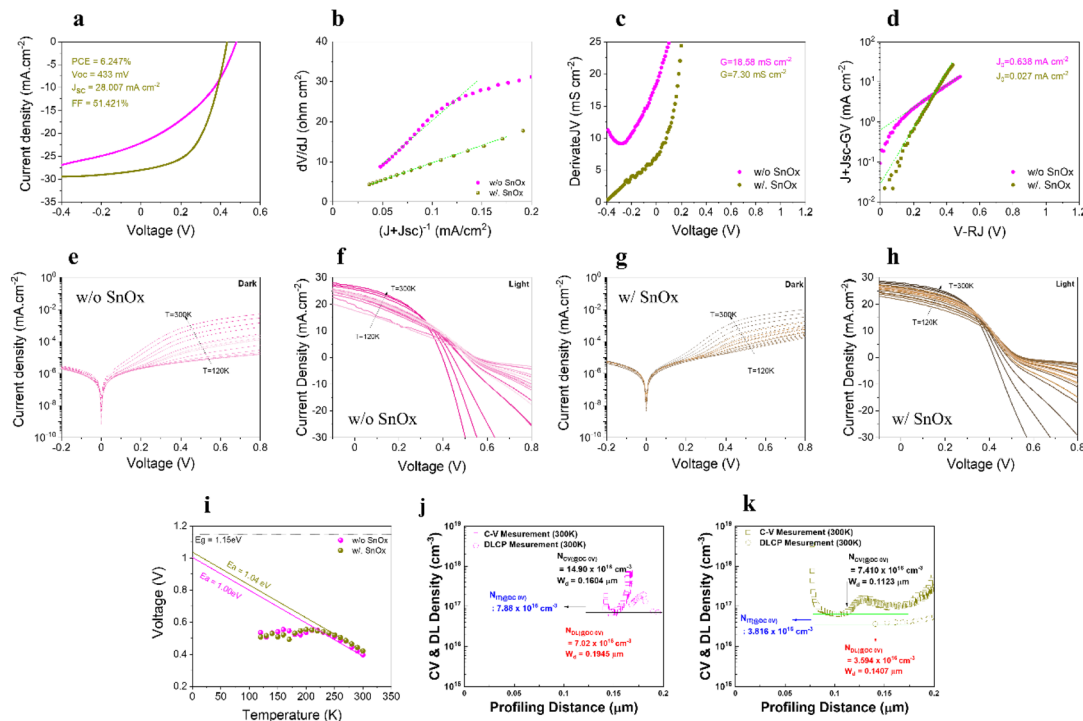


Fig. 6 Characteristic behavior of the best-performing devices: (a)  $J$ - $V$  curves, (b) derivative of  $dV/dJ$  under forward bias with fitting used to determine the series resistance and diode ideality factor, (c) derivative of  $dJ/dV$  for shunt characteristic analysis, and (d)  $\ln(J + J_{\text{sc}} - GV)$  versus  $(V - RJ)$  curves. IVT measurements of  $\text{Sb}_2\text{Se}_3$  devices under light and dark conditions (120 K to 300 K), showing the determination of series and shunt resistance (e and f) without the ALD  $\text{SnO}_x$  interlayer and (g and h) with the ALD  $\text{SnO}_x$  interlayer. (i) Temperature dependence of  $V_{\text{OC}}$ . Capacitance–voltage (C–V) and drive-level capacitance profiling (DLCP) of devices (j) without the ALD  $\text{SnO}_x$  interlayer and (k) with the ALD  $\text{SnO}_x$  interlayer.



boundaries (GBs) can create alternative paths for electron and hole transport, increasing shunt conductance while maintaining a relatively low series resistance. This phenomenon was observed in the  $\text{Sb}_2\text{Se}_3$  device without the  $\text{SnO}_x$  interlayer, resulting in a higher shunt conductance of  $18.58 \text{ mS cm}^{-2}$ , as shown in Table 1. In contrast, the  $\text{Sb}_2\text{Se}_3$  device with the ALD  $\text{SnO}_x$  interlayer exhibited a lower shunt conductance of  $7.30 \text{ mS cm}^{-2}$  due to defect passivation.<sup>39</sup> As shown in Fig. 6d, the loss mechanisms and variations between the ideal and actual performance of the  $\text{SnO}_x$ -based devices were analyzed. The values of  $J_0$  and  $A$  decreased from 0.638 to 0.027 and from 6.10 to 2.08, respectively, due to reduced recombination at the  $\text{Sb}_2\text{Se}_3/\text{CdS}$  interface, attributed to the passivation effect of the ALD  $\text{SnO}_x$  interlayer. The presence of the ALD  $\text{SnO}_x$  interlayer resulted in a lower  $A$ , indicating reduced recombination losses from interface defects. Additionally, the reduced  $J_0$  in the  $\text{Sb}_2\text{Se}_3$  device with  $\text{SnO}_x$  suggests a lower defect density and diminished carrier recombination.

To better understand the impact of the  $\text{SnO}_x$  interlayer on device performance, we investigated the electrical properties of solar cells over a temperature range of 120 K to 300 K. The electrical characteristics of solar cells are intricately linked with photovoltaic performance and serve as an effective means of examining carrier transport and recombination behavior. Fig. 6e–h presents the temperature-dependent IVT curves under dark and illuminated conditions for devices with and without the ALD  $\text{SnO}_x$  interlayer. IVT measurements were conducted for all samples at temperatures ranging from 120 K to 300 K. A more pronounced current-blocking effect on injection current was observed at higher temperatures in the  $\text{Sb}_2\text{Se}_3$  device with the ALD  $\text{SnO}_x$  interlayer compared to the device without  $\text{SnO}_x$ .<sup>56</sup> Fig. 6i presents the temperature dependence of  $V_{\text{OC}}$ , which was analyzed to investigate the recombination characteristics at the  $\text{Sb}_2\text{Se}_3/\text{CdS}$  interface. The activation energy ( $E_A$ ) was figured out by linearly extrapolating the data within the measured  $V_{\text{OC}}$  temperature range (120 K  $< T <$  300 K), with  $E_A$  corresponding to the value at  $T = 0 \text{ K}$ . The  $E_A/E_g$  ratios were 85.47% for the  $\text{Sb}_2\text{Se}_3$  device without  $\text{SnO}_x$  and 88.89% for the device with the ALD  $\text{SnO}_x$  interlayer. An increase in  $E_A/E_g$  correlates with improved photovoltaic performance due to reduced recombination losses from defects at the  $\text{Sb}_2\text{Se}_3/\text{CdS}$  interface (Table 1). The recombination mechanism follows the Shockley–Read–Hall (SRH) process in the space-charge region (SCR) when  $E_A$  is close to  $E_g$ . In contrast, a lower  $E_A/E_g$  suggests recombination at the absorber–buffer interface.<sup>57</sup> Therefore, the ALD  $\text{SnO}_x$  interlayer functioned as a surface passivation layer, mitigating recombination losses at the  $\text{Sb}_2\text{Se}_3/\text{CdS}$  interface.<sup>58</sup>

Fig. 6j and k present carrier density as a function of depletion width, obtained from capacitance–voltage ( $C$ – $V$ ) profiling and drive-level capacitance profiling (DLCP) measurements, to examine the electrical properties near the  $\text{Sb}_2\text{Se}_3/\text{CdS}$  interface. The depletion width ( $W_d$ ) was determined from DLCP measurements by evaluating the capacitance at zero bias and applying the formula  $W_d = \varepsilon_0 \varepsilon A/C$ , where  $C$  is the measured capacitance for each DC bias,  $A$  is the device area ( $0.185 \text{ cm}^2$ ), and  $\varepsilon$  is the dielectric constant of the absorber (fixed at 14.3 in this study based on prior assumptions).<sup>41,59</sup> Carrier density  $N$

**Table 2** Carrier density parameters of  $\text{Sb}_2\text{Se}_3$  solar cells with and without the ALD  $\text{SnO}_x$  interlayer

Samples	$N_{\text{CV}} (\text{cm}^{-3})$	$W_d (\mu\text{m})$	$N_{\text{IT}} (\text{cm}^{-3})$	$N_{\text{DLCP}} (\text{cm}^{-3})$
W/o $\text{SnO}_x$	$14.90 \times 10^{16}$	0.167	$7.88 \times 10^{16}$	$7.02 \times 10^{16}$
w/ $\text{SnO}_x$	$7.41 \times 10^{16}$	0.141	$3.76 \times 10^{16}$	$3.59 \times 10^{16}$

and  $W_d$  were extracted from  $C$ – $V$  profiling and DLCP measurements. The calculated carrier density ( $N_{\text{CV}}$ ), depletion width ( $W_d$ ), interface trap density ( $N_{\text{IT}}$ ), and bulk density ( $N_{\text{DLCP}}$ ) are summarized in Table 2. The  $N_{\text{DLCP}}$  and  $N_{\text{CV}}$  values for the  $\text{Sb}_2\text{Se}_3$  device without the ALD  $\text{SnO}_x$  interlayer were determined to be approximately  $7.02 \times 10^{16} \text{ cm}^{-3}$  and  $14.90 \times 10^{16} \text{ cm}^{-3}$ , respectively. With the ALD  $\text{SnO}_x$  interlayer, these values decreased to approximately  $3.59 \times 10^{16} \text{ cm}^{-3}$  and  $7.41 \times 10^{16} \text{ cm}^{-3}$ , respectively. The high density of traps at the interface indicates an increased recombination rate at the  $\text{Sb}_2\text{Se}_3/\text{CdS}$  interface, which negatively affects device performance due to significant bulk defects in the  $\text{Sb}_2\text{Se}_3$  absorber. Both  $\text{Sb}_2\text{Se}_3$  devices, with and without the ALD  $\text{SnO}_x$  interlayer, exhibited a relatively wide depletion region. The interface trap density ( $N_{\text{IT}}$ ), defined as the difference between  $N_{\text{CV}}$  and  $N_{\text{DLCP}}$  at zero bias, was  $7.88 \times 10^{16}$  for the device without the interlayer and  $3.76 \times 10^{16} \text{ cm}^{-3}$  for the device with the interlayer. This reduction is consistent with the mitigation of interface recombination observed in IVT measurements. The lower  $N_{\text{IT}}$  in the ALD  $\text{SnO}_x$  device confirms the effective passivation of interface traps at the  $\text{Sb}_2\text{Se}_3/\text{CdS}$  junction. The interface defect density was reduced by a factor of 2.09 in the  $\text{SnO}_x$ -treated device, further corroborating that  $\text{SnO}_x$  effectively suppresses recombination centers, leading to improved device performance.

## 2.4 Function of $\text{SnO}_x$ for the nanorod array $\text{Sb}_2\text{Se}_3/\text{CdS}$ interface

To investigate the coverage of CdS buffer layers on the rough surface of  $\text{Sb}_2\text{Se}_3$  absorbers and the interdiffusion of elements at the  $\text{CdS}/\text{Sb}_2\text{Se}_3$  interface, we intentionally fabricated nanostructured  $\text{Sb}_2\text{Se}_3$  absorbers by co-evaporating  $\text{Sb}_2\text{Se}_3$  onto a 30 nm-thick  $\text{MoSe}_2$  layer, which is known to promote the formation of an  $\text{Sb}_2\text{Se}_3$  nanorod array<sup>12</sup> (Fig. S14, SI). As shown in Fig. 7a and b, the introduction of the 30 nm-thick  $\text{MoSe}_2$  layer facilitated the formation of an  $\text{Sb}_2\text{Se}_3$  nanorod array on a flat  $\text{Sb}_2\text{Se}_3$  film. Fig. 7c illustrates the schematic of a nanostructured  $\text{Sb}_2\text{Se}_3$  solar cell incorporating the thick  $\text{MoSe}_2$  layer. Unlike the  $\text{Sb}_2\text{Se}_3$  device with a 5 nm  $\text{MoSe}_2$  layer, depositing a CdS buffer layer with good coverage on the nanorod array of  $\text{Sb}_2\text{Se}_3$  on 30 nm  $\text{MoSe}_2$  was challenging. Incomplete coverage could lead to shunt leakage due to local discontinuities or pinholes at the  $\text{Sb}_2\text{Se}_3/\text{CdS}$  junction. Therefore, the nanostructured  $\text{Sb}_2\text{Se}_3$  absorber required an effective passivation and protection layer to ensure strong adhesion and well-defined junction formation between the  $\text{Sb}_2\text{Se}_3$  absorber and the CdS buffer layer. Fig. S15, SI presents TEM-EDS images of co-evaporated  $\text{Sb}_2\text{Se}_3$  solar cells fabricated with thick  $\text{MoSe}_2$  layers. To address this issue, the ultrathin ALD  $\text{SnO}_x$  interlayer improved contact between the



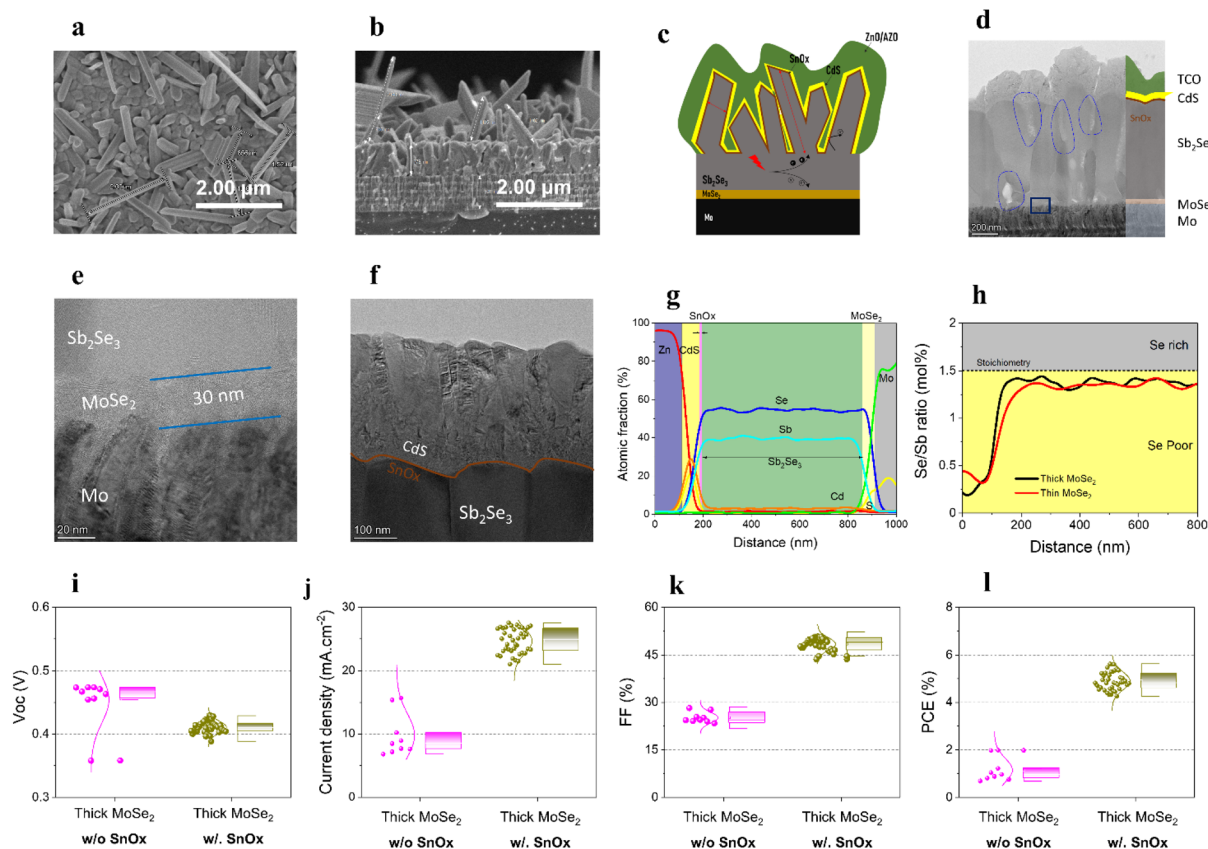
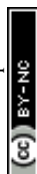


**Fig. 7** (a) Top-view and (b) cross-sectional SEM images of co-evaporated  $\text{Sb}_2\text{Se}_3$  nanorod arrays on a 30 nm-thick  $\text{MoSe}_2/\text{Mo}$  substrate. (c) Schematic illustration of the co-evaporated  $\text{Sb}_2\text{Se}_3$  nanorod array solar cell device. High-resolution cross-sectional TEM (HRTEM) images of (d) the best-performing device, (e) an enlarged HRTEM image of the  $\text{MoSe}_2/\text{Sb}_2\text{Se}_3$  interface (highlighted rectangular region), and (f) the  $\text{Sb}_2\text{Se}_3/\text{CdS}$  interface. (g) EDX line scans of the device and (h) EDX line scans of the Se/Sb ratio in co-evaporated  $\text{Sb}_2\text{Se}_3$  devices with varying  $\text{MoSe}_2$  thicknesses. (i–l) Box plots of the solar cell parameters for co-evaporated  $\text{Sb}_2\text{Se}_3$  nanorod array devices utilizing the thick  $\text{MoSe}_2/\text{Mo}$  substrate.

CdS buffer layer and the rough  $\text{Sb}_2\text{Se}_3$  nanorod array absorber, thereby reducing shunt leakage and potentially enhancing  $J_{\text{SC}}$ . The HRTEM images (Fig. 7d and e) clearly showed a 30 nm-thick  $\text{MoSe}_2$  layer at the interface between Mo and  $\text{Sb}_2\text{Se}_3$ . Further analysis of  $\text{Sb}_2\text{Se}_3$  films grown on 30 nm-thick  $\text{MoSe}_2$  revealed that the CdS buffer layer not only covered the top of the absorber but also penetrated the spaces, conformally coating the sidewalls and valleys (Fig. 7f). Although a high density of nanorods was observed in the  $\text{Sb}_2\text{Se}_3$  absorber grown on thick  $\text{MoSe}_2$  (as seen in the top SEM image), a region with a flat and compact bottom  $\text{Sb}_2\text{Se}_3$  absorber was selected for cross-sectional HRTEM analysis to emphasize the role of the  $\text{MoSe}_2$  layer in facilitating bulk  $\text{Sb}_2\text{Se}_3$  formation. The location and size of voids within the absorber varied depending on the  $\text{MoSe}_2$  thickness. As previously observed, small voids formed at the bottom of the absorber in the thin  $\text{MoSe}_2$ -based structure, whereas voids and larger spaces were distributed throughout the absorber in the thick  $\text{MoSe}_2$ -based structure. Thus, the ALD passivation layer played a crucial role in protecting the absorber in deep and inaccessible regions during the CdS deposition process, thereby preventing shunt effects.

Fig. 7g and h presents an EDX line scan of elemental distribution and the Se/Sb ratio (mol%) in  $\text{Sb}_2\text{Se}_3$  solar cell

devices incorporating the ALD  $\text{SnO}_x$  interlayer with a thick  $\text{MoSe}_2$  layer. The introduction of a 30 nm-thick  $\text{MoSe}_2$  layer induced morphological changes in the  $\text{Sb}_2\text{Se}_3$  absorber while maintaining its chemical composition, as compared to a 5 nm-thick  $\text{MoSe}_2$  layer. This finding indicates that the optical properties and energy band structure of the  $\text{Sb}_2\text{Se}_3$  absorber remained unchanged. To assess the charge extraction and passivation effects of the ALD  $\text{SnO}_x$  interlayer on device performance with a 30 nm-thick  $\text{MoSe}_2$  layer,  $\text{Sb}_2\text{Se}_3$  solar cell devices were fabricated with the structure  $\text{Mo}/\text{MoSe}_2$  (30 nm)/ $\text{Sb}_2\text{Se}_3/\text{SnO}_x/\text{ZnO}/\text{AZO}/\text{Al}$  electrode. As shown in Fig. 7i–l, the best-performing control device exhibited a PCE of 1.971%, with a  $V_{\text{OC}}$  of 0.454 V, a  $J_{\text{SC}}$  of  $15.381 \text{ mA cm}^{-2}$ , and an FF of 28.200%. In comparison,  $\text{Sb}_2\text{Se}_3$  devices incorporating the ALD  $\text{SnO}_x$  interlayer achieved a maximum PCE of 5.627%, with a  $V_{\text{OC}}$  of 0.414 V, a  $J_{\text{SC}}$  of  $27.214 \text{ mA cm}^{-2}$ , and an FF of 49.880% (corresponding values are provided in Table S2). The diode properties of  $\text{Sb}_2\text{Se}_3$  solar cells based on the thick  $\text{MoSe}_2$  layer are shown in Fig. S16 (SI), showing an improvement in diode behavior due to the passivation layer. The incorporation of  $\text{SnO}_x$  at the interface significantly enhanced device performance consistency, even when using inherently rough  $\text{Sb}_2\text{Se}_3$  films, leading to a narrower distribution of PV parameters.



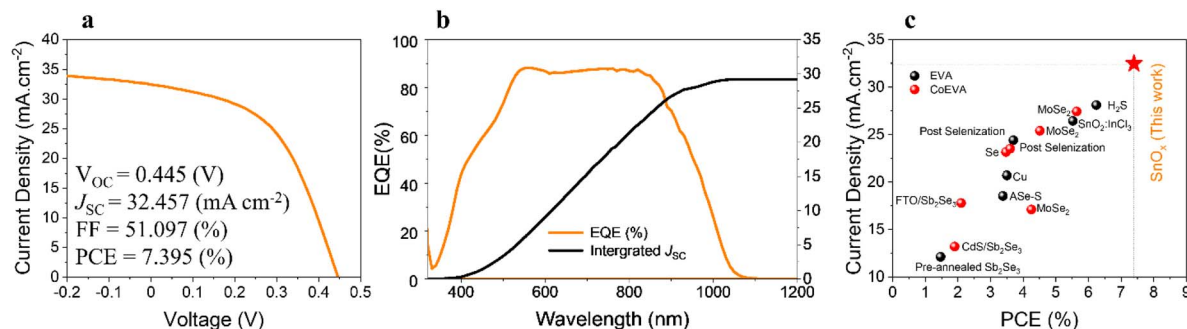


Fig. 8 (a) Current density–voltage ( $J$ – $V$ ) curve and (b) external quantum efficiency (EQE) spectra of the highest-performing  $\text{Sb}_2\text{Se}_3$  solar cells fabricated with a passivation layer. (c) Efficiency distribution of  $\text{Sb}_2\text{Se}_3$  heterojunction solar cells produced using evaporation and co-evaporation methods. An anti-reflective (AR) coating was applied to the device.

Table 3 Detailed photovoltaic performance parameters of high efficiency (co)evaporated  $\text{Sb}_2\text{Se}_3$  devices

Configuration	PCE (%)	$V_{OC}$ (mV)	$J_{SC}$ ( $\text{mA cm}^{-2}$ )	FF (%)	$E_g$ (eV)	Date	Institute
Substrate	1.47	0.407	12.11	30.00	1.20	2018	CNU <sup>60</sup>
Superstrate	1.90	0.300	13.20	48.00		2014	HUST <sup>19</sup>
Superstrate	2.10	0.354	17.80	33.50		2014	HUST <sup>20</sup>
Substrate	3.38	0.362	18.54	50.39		2023	SRMIST <sup>61</sup>
Superstrate	3.47	0.364	23.14	41.26	1.18	2016	HB <sup>22</sup>
Superstrate	3.50	0.339	20.70	49.00		2019	LAPS <sup>62</sup>
Superstrate	3.60	0.352	23.50	44.20		2021	LAPS <sup>23</sup>
Superstrate	3.70	0.335	24.40	46.80		2014	HUST <sup>63</sup>
Substrate	4.25	0.420	17.11	58.15	1.25	2016	HB <sup>21</sup>
Substrate	4.51	0.370	25.39	47.24		2019	DGIST <sup>11</sup>
Superstrate	5.52	0.367	26.44	56.95		2023	USTC <sup>64</sup>
Substrate	5.63	0.430	27.43	47.35		2021	DGIST <sup>12</sup>
Superstrate	6.24	0.380	28.10	59.10	1.13	2020	CUAS <sup>65</sup>
<b>Substrate</b>	<b>7.395</b>	<b>0.445</b>	<b>32.457</b>	<b>51.097</b>	<b>1.17</b>	<b>2024</b>	<b>This work</b>

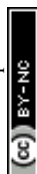
Additionally,  $\text{Sb}_2\text{Se}_3$  solar cells with a 30 nm-thick  $\text{MoSe}_2$  layer showed a reduced variation in photovoltaic parameters, aligning with the previously observed results for  $\text{Sb}_2\text{Se}_3$  devices using a 5 nm-thick  $\text{MoSe}_2$  layer.

The  $\text{Sb}_2\text{Se}_3$  solar cells fabricated on a  $\text{MoSe}_2/\text{Mo}$  substrate at 410 °C for 10 minutes were analyzed by an external certified laboratory to confirm our in-house PCE measurements. The  $J$ – $V$  and EQE curves of the best-performing devices are shown in Fig. 8, with their photovoltaic parameters summarized in Fig. 8a. The device showed an active area efficiency of 7.395% using an anti-reflective magnesium fluoride ( $\text{MgF}_2$ ) coating, with an FF of 51.097%,  $J_{SC}$  of  $32.457 \text{ mA cm}^{-2}$ , and  $V_{OC}$  of 0.445 V. The highest-efficiency  $\text{Sb}_2\text{Se}_3$  device provided a relatively low  $J_0$  value, showing that the passivation layer effectively reduced photo-generated charge carrier losses (Fig. S17, SI). For further comparison, Fig. 8c and Table 3 summarize the PCEs of this work alongside previously reported  $\text{Sb}_2\text{Se}_3$  solar cells fabricated using evaporation-based methods. Notably, this study achieved the highest efficiency among (co)evaporation methods using a substrate configuration. The ultra-high vacuum environment used in the (co)evaporation method, often reaching pressures below  $10^{-7}$  torr, ensures superior interface integrity and significantly mitigates defect formation. This results in higher material quality compared to other

vacuum-based techniques such as close-spaced sublimation (CSS) or atomic layer deposition (ALD), which typically run at lower vacuum levels ( $10^{-2}$  to  $10^{-5}$  torr).

### 3. Conclusions

We reported an effective passivation method for fabricating high-efficiency  $\text{Sb}_2\text{Se}_3$  solar cells using the co-evaporation process. An ultrathin  $\text{SnO}_x$  interlayer, deposited by ALD, was introduced between the  $\text{Sb}_2\text{Se}_3$  absorber and the CdS buffer layer, resulting in improved  $J_{SC}$ , FF, and overall device efficiency. The ALD  $\text{SnO}_x$  interlayer effectively suppressed carrier recombination at the grain interiors and grain boundaries of the  $\text{Sb}_2\text{Se}_3$  absorber while serving as a barrier against Sb element interdiffusion. This passivation of the  $\text{Sb}_2\text{Se}_3/\text{CdS}$  interface led to a significant enhancement in the performance of  $\text{Sb}_2\text{Se}_3$  solar cells, regardless of absorber morphology. Additionally, the conformal deposition of the ALD  $\text{SnO}_x$  interlayer resulted in a uniform device structure, enhancing the reproducibility of co-evaporated  $\text{Sb}_2\text{Se}_3$  solar cells. As a result,  $\text{Sb}_2\text{Se}_3$  solar cells with the ALD  $\text{SnO}_x$  interlayer achieved an efficiency of 7.395%, the highest recorded for co-evaporated  $\text{Sb}_2\text{Se}_3$  devices. Further optimization of the ALD  $\text{SnO}_x$  interlayer could lead to performance improvements.



## 4. Experimental

### 4.1 Preparation of the ALD SnO<sub>x</sub> layer

The SnO<sub>x</sub> deposition was conducted using a custom-built ALD system at 100 °C, with TDMASn as the precursor (supported at 45 °C) and O<sub>3</sub> as the oxidizer. The base pressure was kept at  $3 \times 10^{-2}$  torr, with an added Ar flow of 20 sccm under working conditions. During deposition, ALD-SnO<sub>x</sub> films on Sb<sub>2</sub>Se<sub>3</sub> were heated using a hot trap at 350 °C. The growth rate of SnO<sub>x</sub> was determined to be 0.14 nm per cycle, as confirmed by TEM analysis, which measured a 20 nm thickness on a Si wafer after 140 cycles. The average O/Sn ratio was calculated to be 2.781 based on TEM-EDS measurements (Fig. S18, SI).

### 4.2 Fabrication of the Sb<sub>2</sub>Se<sub>3</sub> device

Solar cells were fabricated as a multilayer stack consisting of soda lime glass (SLG)/Mo/Sb<sub>2</sub>Se<sub>3</sub>/SnO<sub>x</sub>/CdS/i-ZnO/ZnO:Al. The Mo back electrode was deposited onto the SLG substrate *via* DC sputtering. A thin MoSe<sub>2</sub> layer (~5 nm) was grown at  $T_{\text{sub}} = 600$  °C using co-evaporation equipment, while a thicker MoSe<sub>2</sub> layer (30 nm) was deposited at  $T_{\text{sub}} = 430$  °C for 10 min using a two-zone furnace system. The morphology of the three different Mo substrates is illustrated in Fig. S19 (SI). The Sb<sub>2</sub>Se<sub>3</sub> absorber was deposited *via* co-evaporation, using a lower-temperature growth step with  $T_{\text{source}} = 630$  °C and  $T_{\text{sub}} = 315$  °C. The CdS buffer layer was later deposited *via* chemical bath deposition (CBD) at 65 °C for 11.5 min. The device was completed by sputtering a 50 nm i-ZnO layer followed by a 350 nm ZnO:Al layer (sheet resistance  $\approx 30 \Omega \text{ sq}^{-1}$ ). An anti-reflective coating using a magnesium fluoride (MgF<sub>2</sub>) anti-reflective film formed by thermal evaporation deposition was only applied to the best cells in this study. Finally, each sample was sectioned into 16 solar cells (active area = 0.185 cm<sup>2</sup>) by scribing.

### 4.3 Characterization

Surface and cross-sectional images were obtained using a field-emission scanning electron microscope (FESEM; Hitachi S-4800). Elemental mapping of the prepared materials was conducted using scanning transmission electron microscopy with energy-dispersive spectrometry (STEM-EDS). Optical absorption spectra were recorded using a UV-visible spectrophotometer (NEOSYS-2000, SINCO Co., Ltd, Seoul, Korea). X-ray diffraction (XRD) analysis was performed using an Empyrean diffractometer (PANalytical Co.) with CuK $\alpha$  radiation ( $\lambda = 0.15406$  nm) to determine the crystal structure of the films. Raman spectroscopy measurements were conducted using a Raman system equipped with an Mmac 750 spectrometer and a 532 nm excitation laser (irradiation power < 1 mW, spot size 0.7–1  $\mu\text{m}$ ). A 532 nm green laser was used, with its power reduced to 1% using an Nd filter. The laser was focused on the sample surface through a 100 $\times$  magnification lens, and measurements were taken at three locations: left, center, and right of the sample surface. Ultraviolet photoelectron spectroscopy (UPS) spectra were acquired using an ESCALAB 250Xi system (Thermo Scientific Co.) to determine the work function and valence band

maximum of the absorber layer surfaces. The elemental distribution of the thin films was analyzed using secondary ion mass spectrometry (SIMS) (TOF-SIMS 5, ION-TOF GmbH). The sputtering source parameters were O<sup>2+</sup> ions with an energy of 1 keV, a current of 220 nA, an area of  $300 \times 300 \mu\text{m}$ , and a sputtered ion dose density (SPIDD) of  $3.29 \times 10^{18}$  ions per cm<sup>2</sup>. Amplitude modulation (AM)-mode Kelvin probe force microscopy (KPFM) measurements were performed using a commercial scanning probe microscope (n-Tracer, NanoFocus Inc.) under ambient conditions to investigate local electronic properties. The noncontact mode was used to scan the surface with a Pt/Ir-coated tip (Nanocensors Inc.), maintained at a 50 nm lift height. The scan rate was kept below 0.25 Hz to minimize tip damage. A lock-in amplifier (SR830, Stanford Research Systems Co.) provided KPFM feedback, with an applied AC amplitude of 1.0 V. Current-voltage (*I*-*V*) curves were recorded under simulated air mass 1.5 global (AM 1.5G) illumination at 100 mW cm<sup>-2</sup> (1 sun) and 25 °C using a 94022A solar simulator (Newport Co.). External quantum efficiency (EQE) was measured using an SR830 DSP lock-in amplifier system. Temperature-dependent voltage characteristics were analyzed under white light illumination using a source meter (2400, Keithley Co.) with an AM 1.5G spectrum Xe lamp (100 mW cm<sup>-2</sup>, Abet Technology Co.) over a temperature range of 120–300 K. Capacitance-voltage (*C*-*V*) and drive-level capacitance profiling (DLCP) measurements were conducted using an LCR meter (E4980A, Agilent) to estimate space charge width and carrier density.

## Author contributions

S. J. S. and D. H. K. conceived the idea and directed the overall project. V. Q. H. and J. L. fabricated the devices and conducted the characterization. B. K. E. conducted the CdS CBD process. G. L. and W. J. conducted the KPFM measurements and performed data analysis. A. A. and D. H. S. conducted the *C*-*V* and DLCP measurements and performed data analysis. D. H. J., H. J. J., D. K. H., J. K. K., E. C. and K. J. Y. participated in discussing the experimental results. V. Q. H. and S. J. S. wrote the manuscript. All authors discussed the results and commented on the paper.

## Data availability

The data that support the findings of this study are available from the corresponding author (D.-H. Kim, monolithical@dgist.ac.kr) upon reasonable request.

Supplementary information: Extensive material characterization, including structural and morphological analysis (XRD, TEM, SEM), electronic properties (UPS), and the performance metrics (*J*-*V* curves, EQE spectra) of the highest-efficiency devices. See DOI: <https://doi.org/10.1039/d5el00031a>.

## Conflicts of interest

There are no conflicts to declare.



## Acknowledgements

This research was supported by grants from the Korea Institute for Advancement of Technology (KIAT), funded by the Korean government (MOTIE) (No. P0024567), and the National Research Foundation of Korea (NRF), funded by the Korean government (MSIT) (No. RS-2025-02315803, RS-2023-NR076874). This work was also supported by the DGIST R&D programs, funded by the Korean government (MSIT) (No. 25-ET-01, 25-CoE-ET-01). The research at EWU was supported by the Basic Science Research Program through the NRF, funded by the Ministry of Education (No. NRF-2018R1A6A1A03025340) and the Ministry of Science and ICT (No. NRF-2022M3J1A1064229, RS-2024-00355905).

## References

- 1 S. Barthwal, R. Kumar and S. Pathak, *ACS Appl. Energy Mater.*, 2022, **5**, 6545–6585.
- 2 I. Gharibshahian, A. A. Orouji and S. Sharbati, *Sol. Energy*, 2021, **227**, 606–615.
- 3 W. Yang and J. Moon, *J. Mater. Chem. A*, 2019, **7**, 20467–20477.
- 4 Y. Zhao, S. Wang, C. Jiang, C. Li, P. Xiao, R. Tang, J. Gong, G. Chen, T. Chen and J. Li, *Adv. Energy Mater.*, 2022, **12**, 2103015.
- 5 X. Wang, R. Tang, C. Jiang, W. Lian, H. Ju, G. Jiang, Z. Li, C. Zhu and T. Chen, *Adv. Energy Mater.*, 2020, **10**, 2002341.
- 6 Z. Li, X. Liang, G. Li, H. Liu, H. Zhang, J. Guo, J. Chen, K. Shen, X. San and W. Yu, *Nat. Commun.*, 2019, **10**, 125.
- 7 X. Liang, C. Guo, T. Liu, Y. Liu, L. Yang, D. Song, K. Shen, R. E. Schropp, Z. Li and Y. Mai, *Sol. RRL*, 2020, **4**, 2000294.
- 8 S. Rijal, D. B. Li, R. A. Awni, C. Xiao, S. S. Bista, M. K. Jamarkattel, M. J. Heben, C. S. Jiang, M. Al-Jassim and Z. Song, *Adv. Funct. Mater.*, 2022, **32**, 2110032.
- 9 G. Liang, M. Chen, M. Ishaq, X. Li, R. Tang, Z. Zheng, Z. Su, P. Fan, X. Zhang and S. Chen, *Adv. Sci.*, 2022, **9**, 2105142.
- 10 G. Lim, H. K. Park, Y. Wang, S. H. Ji, B. Shin and W. Jo, *J. Phys. Chem. Lett.*, 2024, **15**, 2825–2833.
- 11 S.-N. Park, S.-Y. Kim, S.-J. Lee, S.-J. Sung, K.-J. Yang, J.-K. Kang and D.-H. Kim, *J. Mater. Chem. A*, 2019, **7**, 25900–25907.
- 12 S.-N. Park, S.-Y. Kim, S.-J. Lee, S.-J. Sung, K.-J. Yang, J.-K. Kang and D.-H. Kim, *Mater. Adv.*, 2022, **3**, 978–985.
- 13 K. Li, C. Chen, S. Lu, C. Wang, S. Wang, Y. Lu and J. Tang, *Adv. Mater.*, 2019, **31**, 1903914.
- 14 Z. Duan, X. Liang, Y. Feng, H. Ma, B. Liang, Y. Wang, S. Luo, S. Wang, R. E. Schropp and Y. Mai, *Adv. Mater.*, 2022, **34**, 2202969.
- 15 X. Wen, Z. Lu, X. Yang, C. Chen, M. A. Washington, G.-C. Wang, J. Tang, Q. Zhao and T.-M. Lu, *ACS Appl. Mater. Interfaces*, 2023, **15**, 22251–22262.
- 16 Y. Zhao, S. Wang, C. Li, B. Che, X. Chen, H. Chen, R. Tang, X. Wang, G. Chen and T. Wang, *Energy Environ. Sci.*, 2022, **15**, 5118–5128.
- 17 V.-Q. Hoang, D.-H. Jeon, S.-Y. Kim, J. Lee, D.-H. Son, K.-J. Yang, J.-K. Kang, S.-J. Sung, D.-K. Hwang and D.-H. Kim, *J. Sci.: Adv. Mater. Devices*, 2024, **9**, 100665.
- 18 V.-Q. Hoang, D.-H. Jeon, H. K. Park, S.-Y. Kim, W.-H. Kim, D.-K. Hwang, J. Lee, D.-H. Son, K.-J. Yang and J.-K. Kang, *ACS Appl. Energy Mater.*, 2023, **6**, 12180–12189.
- 19 M. Luo, M. Leng, X. Liu, J. Chen, C. Chen, S. Qin and J. Tang, *Appl. Phys. Lett.*, 2014, **104**, 173904.
- 20 X. Liu, J. Chen, M. Luo, M. Leng, Z. Xia, Y. Zhou, S. Qin, D.-J. Xue, L. Lv and H. Huang, *ACS Appl. Mater. Interfaces*, 2014, **6**, 10687–10695.
- 21 Z. Li, X. Chen, H. Zhu, J. Chen, Y. Guo, C. Zhang, W. Zhang, X. Niu and Y. Mai, *Sol. Energy Mater. Sol. Cells*, 2017, **161**, 190–196.
- 22 Z. Li, H. Zhu, Y. Guo, X. Niu, X. Chen, C. Zhang, W. Zhang, X. Liang, D. Zhou and J. Chen, *Appl. Phys. Express*, 2016, **9**, 052302.
- 23 V. Kumar, E. Artegiani, P. Punathil, M. Bertoncello, M. Meneghini, F. Piccinelli and A. Romeo, *ACS Appl. Energy Mater.*, 2021, **4**, 12479–12486.
- 24 C. Chen and J. Tang, *ACS Energy Lett.*, 2020, **5**, 2294–2304.
- 25 J. Dong, Y. Liu, Z. Wang and Y. Zhang, *Nano Sel.*, 2021, **2**, 1818–1848.
- 26 Y. Zhang, T. Shi, L. Duan, B. Hoex and Z. Tang, *Nano Energy*, 2024, **131**, 110282.
- 27 J. Schmidt, R. Peibst and R. Brendel, *Sol. Energy Mater. Sol. Cells*, 2018, **187**, 39–54.
- 28 P. M. Salomé, B. Vermang, R. Ribeiro-Andrade, J. P. Teixeira, J. M. Cunha, M. J. Mendes, S. Haque, J. Borme, H. Aguas and E. Fortunato, *Adv. Mater. Interfaces*, 2018, **5**, 1701101.
- 29 K. Gao, Q. Bi, X. Wang, W. Liu, C. Xing, K. Li, D. Xu, Z. Su, C. Zhang and J. Yu, *Adv. Mater.*, 2022, **34**, 2200344.
- 30 S. M. George, *Chem. Rev.*, 2010, **110**, 111–131.
- 31 R. L. Puurunen, *J. Appl. Phys.*, 2005, **97**, 121301.
- 32 M. Knez, K. Nielsch and L. Niinistö, *Adv. Mater.*, 2007, **19**, 3425–3438.
- 33 C. Altinkaya, E. Aydin, E. Ugur, F. H. Isikgor, A. S. Subbiah, M. De Bastiani, J. Liu, A. Babayigit, T. G. Allen and F. Laquai, *Adv. Mater.*, 2021, **33**, 2005504.
- 34 S. Lan, W. Zheng, S. Yoon, H. U. Hwang, J. W. Kim, D.-W. Kang, J.-W. Lee and H.-K. Kim, *ACS Appl. Energy Mater.*, 2022, **5**, 14901–14912.
- 35 Y. Zhou, Y. Li, J. Luo, D. Li, X. Liu, C. Chen, H. Song, J. Ma, D.-J. Xue and B. Yang, *Appl. Phys. Lett.*, 2017, **111**, 013901.
- 36 C. Wang, S. Lu, S. Li, S. Wang, X. Lin, J. Zhang, R. Kondrotas, K. Li, C. Chen and J. Tang, *Nano Energy*, 2020, **71**, 104577.
- 37 G. Li, Z. Li, X. Liang, C. Guo, K. Shen and Y. Mai, *ACS Appl. Mater. Interfaces*, 2018, **11**, 828–834.
- 38 K. Shen, C. Ou, T. Huang, H. Zhu, J. Li, Z. Li and Y. Mai, *Sol. Energy Mater. Sol. Cells*, 2018, **186**, 58–65.
- 39 K. Yang, B. Li and G. Zeng, *Sol. Energy Mater. Sol. Cells*, 2020, **208**, 110381.
- 40 D. Ren, B. Fu, J. Xiong, Y. Wang, B. Zhu, S. Chen, Z. Li, H. Ma, X. Zhang and D. Pan, *Adv. Mater.*, 2025, **37**, 2416885.
- 41 C. Chen, W. Li, Y. Zhou, C. Chen, M. Luo, X. Liu, K. Zeng, B. Yang, C. Zhang and J. Han, *Appl. Phys. Lett.*, 2015, **107**, 043905.



- 42 E. Cho, S.-J. Sung, K.-J. Yang, J. Lee, V.-Q. Hoang, B. Kadiri-English, D.-K. Hwang, J.-K. Kang and D.-H. Kim, *J. Mater. Chem. A*, 2025, **13**, 8507–8517.
- 43 S. Dias, B. Murali and S. Krupanidhi, *Sol. Energy Mater. Sol. Cells*, 2015, **143**, 152–158.
- 44 Q. Xie, Z. Liu, M. Shao, L. Kong, W. Yu and Y. Qian, *J. Cryst. Growth*, 2003, **252**, 570–574.
- 45 T. Zhai, M. Ye, L. Li, X. Fang, M. Liao, Y. Li, Y. Koide, Y. Bando and D. Golberg, *Adv. Mater.*, 2010, **22**, 4530–4533.
- 46 Z. Cai, B. Che, Y. Gu, P. Xiao, L. Wu, W. Liang, C. Zhu and T. Chen, *Adv. Mater.*, 2024, **36**, 2404826.
- 47 S. K. Kim, H. K. You, K. R. Yun, J. H. Kim and T. Y. Seong, *Adv. Opt. Mater.*, 2023, **11**, 2202625.
- 48 N. Ahmad, Y. Zhao, F. Ye, J. Zhao, S. Chen, Z. Zheng, P. Fan, C. Yan, Y. Li and Z. Su, *Adv. Sci.*, 2023, **10**, 2302869.
- 49 W. Yang, J. H. Kim, O. S. Hutter, L. J. Phillips, J. Tan, J. Park, H. Lee, J. D. Major, J. S. Lee and J. Moon, *Nat. Commun.*, 2020, **11**, 861.
- 50 Y. M. Lee, B. K. Jung, J. Ahn, T. Park, C. Shin, T. N. Ng, I. S. Kim, J. H. Choi and S. J. Oh, *Adv. Electron. Mater.*, 2022, **8**, 2200297.
- 51 A. Chen and K. Zhu, *Sol. Energy*, 2014, **107**, 195–201.
- 52 C. Otalora, M. Botero and G. Ordonez, *J. Mater. Sci.*, 2021, **56**, 15538–15571.
- 53 N. Maticiu, A. Katerski, M. Danilson, M. Krunk and J. Hiie, *Sol. Energy Mater. Sol. Cells*, 2017, **160**, 211–216.
- 54 R. Ortega-Borges and D. Lincot, *J. Electrochem. Soc.*, 1993, **140**, 3464.
- 55 L. Protesescu, M. Nachttegaal, O. Voznyy, O. Borovinskaya, A. J. Rossini, L. Emsley, C. Copéret, D. Günther, E. H. Sargent and M. V. Kovalenko, *J. Am. Chem. Soc.*, 2015, **137**, 1862–1874.
- 56 T. P. Weiss, S. Nishiwaki, B. Bissig, R. Carron, E. Avancini, J. Löckinger, S. Buecheler and A. N. Tiwari, *Adv. Mater. Interfaces*, 2018, **5**, 1701007.
- 57 S. Kim, J. Lee, D.-H. Son, W. H. Kim, S.-J. Sung, D.-K. Hwang, T. E. Hong, N. Ogtontamir, E. Enkhbayar and T.-H. Lee, *Energy Environ. Sci.*, 2024, **17**, 8609–8620.
- 58 T. K. Todorov, J. Tang, S. Bag, O. Gunawan, T. Gokmen, Y. Zhu and D. B. Mitzi, *Adv. Energy Mater.*, 2013, **3**, 34–38.
- 59 K. Zeng, D.-J. Xue and J. Tang, *Semicond. Sci. Technol.*, 2016, **31**, 063001.
- 60 D. Lee, J. Y. Cho and J. Heo, *Sol. Energy*, 2018, **173**, 1073–1079.
- 61 A. K. Jain, R. Anandan and P. Malar, *Mater. Res. Express*, 2023, **10**, 105502.
- 62 V. Kumar, E. Artegiani, A. Kumar, G. Mariotto, F. Piccinelli and A. Romeo, *Sol. Energy*, 2019, **193**, 452–457.
- 63 M. Leng, M. Luo, C. Chen, S. Qin, J. Chen, J. Zhong and J. Tang, *Appl. Phys. Lett.*, 2014, **105**, 083905.
- 64 L. Huang, J. Yang, Y. Xia, P. Xiao, H. Cai, A. Liu, Y. Wang, X. Liu, R. Tang and C. Zhu, *J. Mater. Chem. A*, 2023, **11**, 16963–16972.
- 65 S. Yao, J. Wang, J. Cheng, L. Fu, F. Xie, Y. Zhang and L. Li, *ACS Appl. Mater. Interfaces*, 2020, **12**, 24112–24124.

